PCCP

ROYAL SOCIETY OF CHEMISTRY

PAPER

View Article Online
View Journal | View Issue

Cite this: *Phys. Chem. Chem. Phys.*, 2024, **26**, 5597

An effective method in modulating thermally activated delayed fluorescence (TADF) emitters from green to blue emission: the role of the phenyl ring†

Lijuan Wang, Zhongqi Ge, Lin Xu and Yan Song *

Developing efficient blue emitters with high performance and low cost is crucial for the further development of organic light-emitting diodes (OLEDs). Based on the two experimentally reported green thermally activated delayed fluorescence (TADF) emitters, which are thioxanthone derivatives consisting of carbazole as an electron donor and 9*H*-thioxanthen-9-one-*S*,*S*-dioxide (SOXO) as an electron acceptor with donor–acceptor (D–A) or donor–acceptor–donor (D–A–D) structures, two new blue TADF emitters are designed by simply inserting a phenyl ring between D and A units. The TADF processes of the four thioxanthone derivatives are studied systematically through first-principles calculations. The role of the introduced phenyl ring in the excited state properties of the designed molecules is explored by analyzing the changes in molecular geometries, frontier molecular orbital distributions, the lowest singlet–triplet energy splitting (ΔE_{ST}), the spin orbit coupling (SOC) constants, the radiative decay rates (k_r) and the nonradiative decay rates (k_{nr}), as well as the intersystem crossing rates (k_{ISC}) and reverse intersystem crossing rates (k_{RISC}). The results show that when incorporating phenyl units into the D–A and D–A–D structures, both high k_r and enhanced k_{RISC} are achieved in **Cz-Ph-SOXO** and **DCz-DPh-SOXO**, demonstrating that incorporating the phenyl unit in D–A and D–A–D structures is an efficient way for developing new SOXO-based TADF molecules. It is worth noting that the k_{RISC} values for **Cz-Ph-SOXO** and **DCz-DPh-SOXO** are significantly increased with respect to those of the experimental molecules. The present results would provide helpful guidelines for developing new SOXO-based TADF molecules experimentally.

Received 20th November 2023,
Accepted 16th January 2024

DOI: 10.1039/d3cp05632e

rsc.li/pccp

1. Introduction

As the third generation of organic light emitting diode (OLED) emitters, thermally activated delayed fluorescence (TADF) materials, which can harvest both the singlet and triplet excitons through the efficient reverse intersystem crossing (RISC) process, have drawn more and more attention in recent years.[1–3] Unlike the conventional fluorescent and phosphorescent materials, the TADF emitters can utilize all the singlet and triplet excitons and realize high efficiency without the assistance of noble metals. Thus, there is a high potentiality to develop lower cost, but more promising OLED devices based on this class of materials. For an efficient TADF emitter, two key parameters, a small singlet–triplet energy splitting (ΔE_{ST}) and high photoluminescence quantum yield (Φ_{PL}), are requisite.[4–7] To achieve a small ΔE_{ST}, the spatial separation of the highest occupied molecular orbital (HOMO) and the lowest unoccupied molecular orbital (LUMO) of the molecules are required and thereby the exchange integral (J) will be reduced based on the equation $\Delta E_{ST} = 2J = 2\int\int \phi_L(1)\phi_H(2)\left(\frac{e^2}{r_1 - r_2}\right)\phi_L(2)\phi_H(1)\mathrm{d}r_1\,\mathrm{d}r_2$.[8,9] However, the demand of the separated distribution of the HOMO/LUMO for a narrow ΔE_{ST} can suppress the transition dipole moment between the ground state (S_0) and the first singlet excited state (S_1), leading to a small oscillator strength (f) and low Φ_{PL}. Therefore, the delicate balance between the spatial separation of the HOMO–LUMO wave function and the large f could be a compromise design strategy for efficient TADF emitters.[4–7] So far, versatile molecular systems with TADF properties have been developed, including spiro-acidine,[10] triazine,[11] spirobifluorene,[12] phthalonitrile,[13] triptycene,[8] diphenyl sulfone derivatives,[14–17] and so on. Highly efficient sky-blue OLEDs with 37% external quantum efficiency have been achieved, which can be comparable to the excellent performance of phosphorescent OLEDs.[18] Despite significant

School of Materials Science and Engineering, Harbin Institute of Technology at Weihai, 2 West Wenhua Road, Weihai, 264209, China. E-mail: sy@hitwh.edu.cn

† Electronic supplementary information (ESI) available. See DOI: https://doi.org/10.1039/d3cp05632e

progress having been made in recent years, developing highly efficient new TADF emitters with both small ΔE_{ST} and high Φ_{PL} is still a great challenge. The traditional design strategy for TADF emitters is combining an electron donor (D) and an electron acceptor (A) unit to spatially separate the HOMOs and LUMOs.[19,20] Generally, a phenyl linker is demanded to increase the D–A spatial separation distance and relieve the twisted angle between the D and the A.[21,22] Compared with the D–A-type TADF emitters, D–A–D-type TADF emitters can facilitate a stronger intramolecular charge transfer and therefore smaller ΔE_{ST}, which can promote the highly efficient RISC progress and achieve excellent OLED performance.[23–31]

Thioxanthone (TXO) and 9-*H*-thioxanthen-9-one-10,10-dioxide (SOXO) units are excellent acceptor units for constructing highly efficient TADF materials. The ΔE_{ST} of SOXO is reported to be lower than 0.3 eV,[32,33] and the SOXO core contains a ketone moiety which is alone able to produce delayed fluorescence.[34,35] Several kinds of SOXO systems have been reported to exhibit excellent TADF properties. In 2014, Wang and co-workers reported two efficient TADF emitters of SOXO based derivatives with the D–A structure, using SOXO as the electron acceptor unit, and triphenylamine (TPA)/*N*-phenylcarbazole (PhCz) as the electron donor unit.[36] Later on, they demonstrated a remarkable divergence in the photophysical properties of the SOXO based TADF emitters with different substitution positions of the PhCz donor.[37] In 2019, they designed four D–A–D region isomers with TADF properties by connecting two PhCz as donors at the different substituted positions of the phenyl group in the SOXO unit, highlighting the beneficial role of the different substituted positions of the acceptor unit in facilitating the adjustment of ΔE_{ST} and f.[38] In 2016, Su *et al.* investigated the structure–performance relationship of thioxanthone-based TADF emitters with substituted carbazole donors and inferior OLED performance was achieved for the symmetric D–A–D molecules with 2,7-substitutions.[27] Interestingly, in the same year, they reported blue and yellow TXO-based TADF emitters with the D–A–D structure with an external quantum efficiency (EQE) of over 20%, in which they introduced two triphenylamine (TPA) donor units at the 3 and 6 position of the TX (9-*H*-thioxanthen-9-one) unit. Ultrahigh EQE values of 23.7% and 24.3% are achieved for the symmetrical blue emitter 3,6-2TPA-TX and the yellow emitter 3,6-2TPA-TXO, respectively.[39] Although the SOXO-based TADF emitters have achieved excellent performance in OLED devices, the electroluminescence mechanism of this kind of material is still unclear. For the singlet-harvesting mechanism, both the singlet and triplet excited states are involved in the emission process, and the overall emission behavior relates to the individual properties of these states, ΔE_{ST}, f, the spin orbit coupling (SOC) and the related intersystem crossing (ISC) and RISC processes. All of these properties should be considered sufficiently when engineering the chemical structures of the TADF emitters.[9,40,41] Therefore, a detailed understanding of the structural–property relationship of the organic TADF emitters is crucial for effective materials engineering, which facilitates the development of new efficient TADF emitters and promotes their applications in OLEDs.

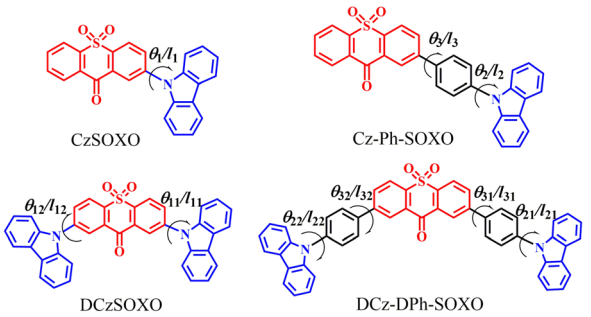

Fig. 1 Chemical structures of the studied thioxanthone-based molecules with D–A (**CzSOXO**), D–π–A (**Cz-Ph-SOXO**), D–A–D (**DCzSOXO**) and D–π–A–π–D (**DCz-DPh-SOXO**) structures, θ and l denote the main dihedral angles and bond lengths.

In this work, the electroluminescence mechanisms of two experimentally reported D–A and D–A–D type SOXO based TADF emitters (the chemical structures are plotted in Fig. 1) are systematically investigated using density functional theory (DFT) and time-dependent density functional theory (TD-DFT). Two new SOXO derivatives are designed *via* simply introducing the phenyl ring between donor and acceptor units with D–π–A and D–π–A–π–D structures to further establish the structure–property relationship. The influence of the phenyl ring on the excited state properties of the SOXO-based molecules is investigated. The photophysical properties, the radiative and nonradiative decay rates, the ISC and RISC rates, as well as SOC constants of the investigated molecules, are explored in detail. It was found that the TADF emitters are modulated from green to blue emission, and the radiative decay rates and the rates of the RISC process are also enhanced through simply incorporating phenyl rings into the experimental molecules.

2. Theoretical methods

The decay rate constants from the S_1 to S_0 states and the interconversion rate constants between the S_1 and T_1 states are key parameters in determining the electroluminescence mechanism of the SOXO-based TADF molecules. The radiative decay rate k_r is calculated by the Einstein spontaneous emission equation as follows:[42–44]

$$k_r = \frac{f\Delta E_{fi}{}^2}{1.499} \quad (1)$$

where f is the oscillator strength and ΔE_{fi} is the vertical emission energy with the unit of wavenumber (cm^{-1}).

The nonradiative decay rate k_{nr} can be obtained based on Fermi's golden rule and the first-order perturbation theory[45,46]

$$k_{nr} = \frac{2\pi}{\hbar^2}\sum_{u,v} P_{iv}\left|\hat{H}_{fu,iv}\right|^2 \delta(E_{iv} - E_{fu}) \quad (2)$$

Here, the delta function δ is to ensure the conservation of energy; P_{iv} is the Boltzmann distribution function for the initial vibronic manifold; $\hat{H}_{fu,iv}$ is the interaction operator between two different Born–Oppenheimer states, consisting of two

contributions as below[46]

$$\hat{H}\Psi_{iv} = \hat{H}^{BO}\Phi_i(r,Q)\Theta_{iv}(Q) + \hat{H}^{SO}\Phi_i(r,Q)\Theta_{iv}(Q) \quad (3)$$

here, $\hat{H}^{BO}$ is the nonadiabatic coupling and $\hat{H}^{SO}$ is the spin–orbit coupling, r and Q are the electronic and normal mode coordinates. Φ_i is the electron wave function, and Θ_{iv} is the nuclear vibrational wave function.

The internal conversion rate constant between two electronic states with the same spin multiplicity can be evaluated by using the first-order perturbation theory as[45]

$$k_{IC} = \frac{1}{\hbar^2}R_{kl}\int_{-\infty}^{\infty} dt\, e^{i\omega_{if}t}\rho_{fi}^{ic}(t,T) \quad (4)$$

Here, the nonadiabatic electronic coupling matrix element $R_{kl} = \langle\Phi_f|\hat{P}_{fk}|\Phi_i\rangle\langle\Phi_i|\hat{P}_{fl}|\Phi_f\rangle$, $\hat{P}_{fk} = -i\hbar\frac{\partial}{\partial Q_{fk}}$ is the normal momentum operator of the k_{th} normal mode in the final electronic states. Φ_f and Φ_i are the wavefunctions of the final state and the initial states, respectively. ρ_{fi}^{ic} is the thermal vibration correlation function (TVCF),[42–44] which is $Z_i^{-1}\,\mathrm{Tr}\left[\hat{P}_{fk}e^{-i\tau_f\hat{H}_f}\hat{P}_{fl}e^{-i\tau_i\hat{H}_i}\right]$. Here, Z_i represents the partition function.

The intersystem crossing rate constant between the singlet and triplet states can be evaluated based on the following equation:[42,43]

$$k_{ISC} = \frac{1}{\hbar}\langle\Phi_f|\hat{H}^{SO}|\Phi_i\rangle\int_{-\infty}^{\infty} dt\left[e^{i\omega_{if}t}Z_i^{-1}\rho_{ISC}(t,T)\right] \quad (5)$$

The detailed derivation of these equations can be found in Peng and Shuai's work.[45–47]

3. Computational details

The geometric optimizations and frequency calculations of the S_0 states are performed *via* density functional theory (DFT), while the excited singlet and triplet states are optimized through the time-dependent DFT (TD-DFT) approach. Since the excited state properties of TADF molecules with charge transfer character are functional dependent, several exchange–correlation functionals, including B3LYP,[48] PBE0,[49] PBE0-1/3,[50] BMK[51] and M062X[52] with different HF exchange percentages in the XC functional of 20%, 25%, 33.33%, 42% and 54%, and two range-separated hybrid functionals, CAM-B3LYP[53] and ωB97XD,[54] are used to calculate the absorption and emission wavelengths of **CzSOXO** and **DCzSOXO** combining with the 6-31G(d)[55–57] basis set (see Table 1). It was shown that the results based on the PBE0-1/3 functional agree well with the experimental values. The PBE0-1/3 functional and 6-31G(d) basis sets are therefore used to evaluate the ground and excited state properties of the studied molecules. All calculations are performed in a toluene solvent with the Polarizable Continuum Model (PCM)[58] using the Gaussian 09 software package.[59]

Based on the electronic properties, the calculations of the radiative and nonradiative decay rates, as well as the intersystem crossing rate and reverse intersystem crossing rate constants are finished through the Molecular Material Property Prediction Package (MOMAP).[60–65] The SOC matrix elements are computed from the quadratic response function by the Dalton program package.[66,67]

Table 1 The calculated absorption (λ_{ab}) and emission (λ_{em}) wavelengths of **CzSOXO** and **DCzSOXO** based on different functionals, together with the experimental values for comparison

	CzSOXO		**DCzSOXO**	
	λ_{ab} (nm)	λ_{em} (nm)	λ_{ab} (nm)	λ_{em} (nm)
B3LYP	521	700	543	730
PBE0	478	617	498	642
PBE0-1/3	423	524	440	542
BMK	393	474	408	476
M062X	361	421	372	425
CAM-B3LYP	352	411	364	415
ωB97XD	341	389	349	395
Expt.[26]	404	536	406	546

In addition, to characterize the geometric changes between the S_0 and S_1 states and between the S_1 and T_1 states, the root of the mean of squared displacement (RMSD) is calculated using the following equation:

$$RMSD = \sqrt{\frac{1}{N}\sum_{i}^{n_{atom}}\left[(x_i - x_i')^2 + (y_i - y_i')^2 + (z_i + z_i')^2\right]} \quad (6)$$

where i is the atomic ordinal number. To analyze the excitation properties of the investigated molecules, the electron–hole (e–h) distributions and the overlaps of e–h of the S_1 states are calculated through the Multiwfn[68,69] software.

4. Results and discussions

4.1 Molecular geometric structures

The molecular geometric structures play a crucial role in determining both the electronic structures and photophysical properties. A large distorted dihedral angle between D and A units generally allows efficient spatial separation of the HOMO and the LUMO to achieve a small ΔE_{ST} value. The geometric structures of the S_0, S_1 and excited triplet states for all the investigated molecules are optimized based on the PBE0-1/3/6-31G(d) level in a toluene solvent. The main dihedral angles and bond lengths (as shown in Fig. 1) of **CzSOXO**, **DCzSOXO**, **Cz-Ph-SOXO** and **DCz-DPh-SOXO** based on the optimized S_0, S_1 and T_1 geometries in toluene are listed in Table 2. It can be seen that the molecular geometries between the S_0 and S_1 states are significantly altered when changing the molecular types. In the S_0 states, the dihedral angle (θ_1) between D and A moieties of **CzSOXO** is 50°, which is almost the same as that of **DCzSOXO**. However, when inserting the phenyl rings between the D and A unit in **CzSOXO** and **DCzSOXO**, the dihedral angles between the SOXO group and the phenyl ring are decreased to 37° for **Cz-Ph-SOXO** and **DCz-DPh-SOXO**, respectively. The corresponding bond lengths (l_1) are also 0.08 Å larger than those of **CzSOXO** and **DCzSOXO**. When comparing the dihedral angles in Table 2 between the S_0 and S_1 states, it can be found that the dihedral angles between D and A units are increased by around 14° for **CzSOXO** and **DCzSOXO**. While the largest

Table 2 The main dihedral angles (in degree) and bond lengths (in angstrom) of the designed SOXO-based molecules based on the optimized S_0 and S_1 geometries in toluene

Molecules	Bond parameters	S_0 geometry	S_1 geometry	T_1 geometry
CzSOXO	θ_1	50	64	42
	l_1	1.40	1.43	1.38
DCzSOXO	θ_{11}/θ_{12}	49/49	64/53	49/43
	l_{11}/l_{12}	1.40/1.40	1.43/1.41	1.40/1.38
Cz-Ph-SOXO	θ_3/θ_2	37/54	33/48	46/2
	l_3/l_2	1.48/1.41	1.47/1.40	1.41/1.39
DCz-DPh-SOXO	$\theta_{31}/\theta_{32}/\theta_{21}/\theta_{22}$	36/37/53/126	35/33/56/132	4/36/46/126
	$l_{31}/l_{32}/l_{21}/l_{22}$	1.48/1.48/1.41/1.41	1.48/1.47/1.41/1.40	1.41/1.48/1.39/1.41

dihedral angle deviations between the S_0 and S_1 states for **Cz-Ph-SOXO** and **DCz-DPh-SOXO** have occurred between the carbazole unit and the inserted phenyl ring, and the value at S_1 states is decreased by 6° with respect to those of S_0 states. The decreased dihedral angles at S_0 and S_1 states make the geometries of **Cz-Ph-SOXO** and **DCz-DPh-SOXO** become more planar compared with those of **CzSOXO** and **DCzSOXO**. It can also be found that the T_1 geometries of the studied molecules change significantly compared with the S_1 geometries, and the selected dihedral angles of **Cz-Ph-SOXO** and **DCz-DPh-SOXO** at the T_1 state show greater changes than those of **CzSOXO** and **DCzSOXO** with respect to those at the S_1 state.

To quantitatively characterize the geometry changes between S_0 and S_1 states and between S_1 and T_1 states, the RMSD analysis of the investigated molecules is performed and the results are presented in Fig. 2. It can be found that the RMSD values between S_0 and S_1 states for **CzSOXO** and **DCzSOXO** are 0.344 and 0.394 Å, respectively. When bringing the phenyl ring between D and A units, the RMSD values decrease to 0.118 and 0.122 Å, respectively. The geometric changes between S_1 and T_1 states show much larger RMSD values than those between S_0 and S_1 states. The large geometry changes will lead to large reorganization energy between the corresponding two states and consequently lead to larger nonradiative decay rates. The geometry changes of the ground state and the excited states *via* changing the molecular types will definitely affect the distributions of the frontier molecular orbitals and the photophysical properties as discussed below.

4.2 Frontier molecular orbitals

The distributions of the frontier molecular orbitals play an important role in determining ΔE_{ST}, which is closely related to the steric hindrance of the molecular geometry. The more separated distributions between HOMOs and LUMOs, the smaller ΔE_{ST} will be. On the other hand, the spatial overlap between HOMO and LUMO is essential to achieve high radiative decay rates (k_r). The distributions and energy levels of HOMOs and LUMOs for the investigated molecules in the S_0 state are plotted in Fig. 3. It can be clearly seen that the HOMOs of **CzSOXO** and **DCzSOXO** are predominantly located on the donor units, and partially on the acceptor groups, and the LUMOs are mainly distributed on the acceptor moieties, and a small portion is distributed on the donor unit, ensuring a partial overlap between the distributions of HOMOs and LUMOs. When inserting the phenyl ring between D and A groups, smaller overlaps between HOMOs and LUMOs for **Cz-Ph-SOXO** and **DCz-DPh-SOXO** can also be found, which facilitates obtaining small ΔE_{ST}. It can also be found that the energy gaps between HOMOs and LUMOs for **Cz-Ph-SOXO** and **DCz-DPh-SOXO** are decreased by 0.14 and 0.10 eV compared with **CzSOXO** and **DCzSOXO**, respectively.

To analyze the excitation properties and quantitatively predict the degree of overlap between HOMOs and LUMOs, the electron–hole (e–h) distribution and overlap of e–h for the S_1 state of the investigated molecules are provided in Fig. 4. It can be seen that there are obvious overlaps of e–h for **CzSOXO** and **DCzSOXO**, mainly occurring on the acceptor unit. For the designed molecules **Cz-Ph-SOXO** and **DCz-DPh-SOXO**, the e–h

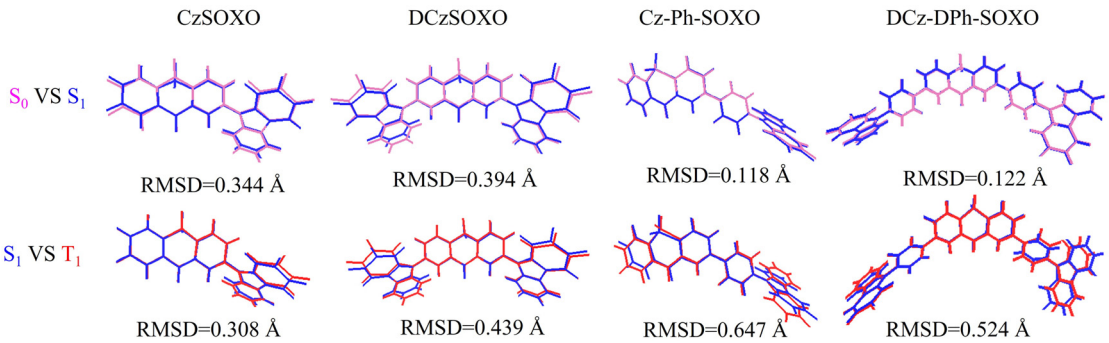

Fig. 2 Comparison of the geometries between S_0 (pink), S_1 (blue) and T_1 (red) states in toluene for investigated molecules (RMSD values are presented).

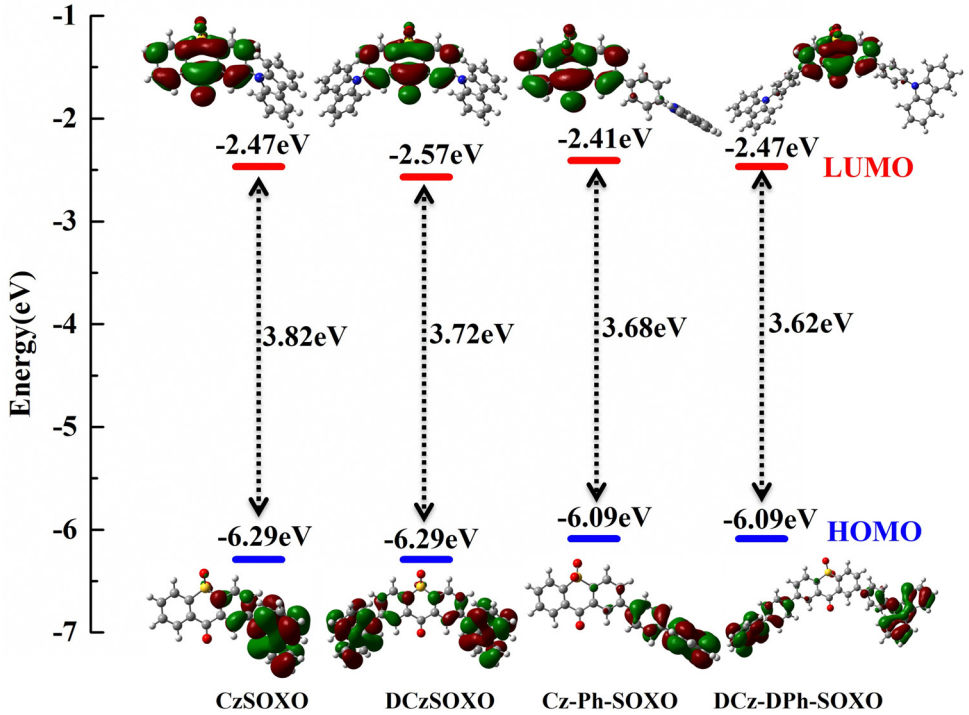

Fig. 3 The distributions and energy levels of the frontier molecular orbitals for the studied molecules at the S_0 state (isovalue is 0.02).

overlap became smaller than those of **CzSOXO** and **DCzSOXO**, indicating that they may possess smaller ΔE_{ST}. It can also be noticed that the e–h distributions are separated significantly for all the investigated molecules, indicating that the charge

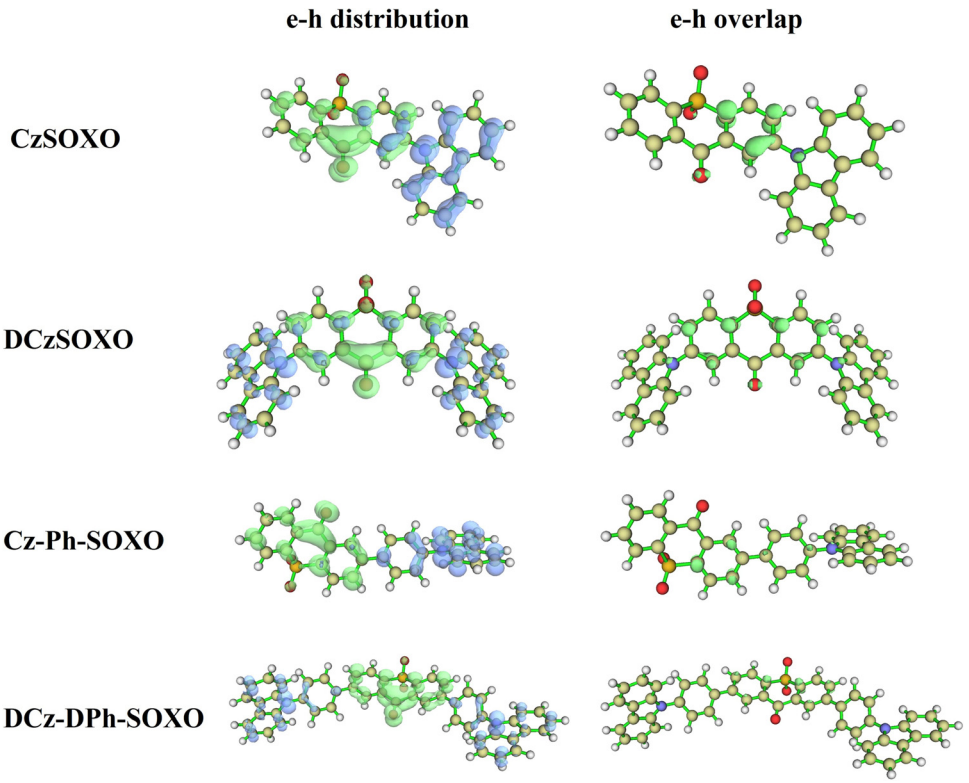

Fig. 4 The electron–hole (e–h) distributions and overlaps of e–h for the S_1 states of **CzSOXO**, **DCzSOXO**, **Cz-Ph-SOXO** and **DCz-DPh-SOXO** (isosurface value is 0.002).

Table 3 The S_r, D, t, H, and Δr index of the investigated molecules

Molecules	S_r/a.u.	D/Å	t/Å	H/Å	Δr_{S_1}/Å	Δr_{S_2}/Å
CzSOXO	0.32	5.08	4.62	2.81	5.66	6.49
DCzSOXO	0.38	1.44	0.08	4.40	1.58	1.62
Cz-Ph-SOXO	0.24	8.75	6.26	3.15	9.50	4.45
DCz-DPh-SOXO	0.29	3.52	1.78	6.02	4.88	4.94

transfer process can occur in all the molecules. To further analyze the inside mechanisms, the spatial separation of holes and electrons S_r, the charge transfer (CT) length D, the degree of separation of holes and electrons t, the reflection of the overall average distribution breadth of electrons and holes H, and the Δr index for the S_1 and S_2 states used to measure the charge transfer length during the electron excitation, are calculated *via* Multiwfn software[68] and the results are listed in Table 3. The calculated parameters in Table 3 also verify the above findings. When the t index is larger than zero, this implies that the distributions of holes and electrons are effectively separated because of the CT process. The Δr index for the S_1 and S_2 states is used to measure the charge transfer length during the electron excitation, and the larger the Δr value is, the more likely the excitation is a CT mode. It can be found that the S_r index of **CzSOXO** (0.32) and **DCzSOXO** (0.38) is larger than **Cz-Ph-SOXO** (0.24) and **DCz-DPh-SOXO** (0.29), indicating the larger overlap between holes and electrons, which is in accord with the e–h distributions as discussed above. It can also be found that t indices are all greater than zero, suggesting that sufficient hole and electron separations occurred in these molecules due to the CT process. However, the t index of **DCzSOXO** is as small as 0.08, demonstrating that there is some overlap between the hole and the electron. For the S_1 and S_2 states, Δr of all the molecules is larger than the threshold distinguishing the local excited (LE) state and the CT excited states of 2 Å, except that of **DCzSOXO**, indicating that they are LE states. It is also illustrated in Table 3 that the e–h overlaps can be decreased when incorporating the phenyl ring in **Cz-Ph-SOXO** and **DCz-DPh-SOXO** with respect to those of **CzSOXO** and **DCzSOXO**.

4.3 ΔE_{ST} and transition properties

The singlet–triplet energy gap (ΔE_{ST}) for TADF molecules is one of the key parameters for the RISC process, which is correlated to the distributions of the HOMO and the LUMO. The excitation energies of S_1 and T_1 states based on the S_0, S_1 and T_1 geometries and the vertical and adiabatic energy splitting between the S_1 and T_1 states for the investigated molecules are provided in Table 4. It can be noticed that the adiabatic energy gaps between the S_1 and T_1 states for **CzSOXO** and **DCzSOXO** are 0.35 and 0.31 eV, respectively. When inserting the phenyl ring between D and A units in **CzSOXO** and **DCzSOXO**, these values are increased to 0.63 and 0.59 eV, respectively. The results are in agreement with the analysis of the geometric changes. However, the energy gap of **Cz-Ph-SOXO** between the T_3 and S_1 states is much smaller than that of **CzSOXO** between T_1 (T_2) and S_1 states (see Fig. 5), demonstrating that the ISC and the RISC processes may occur from the S_1 to T_3 states for **Cz-Ph-SOXO**. Similarly, for **DCzSOXO** and **DCz-DPh-SOXO**, the nearest triplet states to the S_1 state are T_2 (T_3) and T_3 (T_4) states, respectively. So, the ISC process may occur from S_1 to T_2 (T_3) and T_3 (T_4) states, respectively.

The transition properties of excited states are also vital in determining the excited state properties. The natural transition orbital (NTO) analyses of the S_1 and T_1 states in toluene are performed for the investigated molecules. As shown in Fig. S1–S4 (ESI†), the highest occupied natural transition orbital (hole) and the lowest unoccupied natural transition orbital (particle) predominate the transition for S_1 and T_1 states. The S_1 states of the studied molecules generally exhibit charge transfer (CT) characters. For the T_1 and higher triplet states (T_2, T_3 or T_4 states), it can be found that all the molecules not only show significant local excited (LE) properties, but also partial CT characters. The CT characters can help to achieve larger k_{RISC}, therefore realizing a more efficient RISC process.[22]

4.4 Photophysical property

The photophysical property is vital in exploring the TADF process of the investigated molecules. The absorption and emission wavelength as well as the oscillator strength of the S_1 state in a toluene solvent are provided in Table 5, together with the available experimental data. It can be found that the deviation between the theoretical and experimental absorption wavelengths of **CzSOXO** and **DCzSOXO** is less than 34 nm (with a relative difference of 7.7%). The calculated emission wavelengths are also in good agreement with the experimental results, and the deviations are within 12 nm. The emission wavelengths of **CzSOXO** and **DCzSOXO** are 524 and 542 nm, respectively, which are green emitters. While introducing the phenyl rings between the D and the A to **CzSOXO** and **DCzSOXO** make the emission wavelengths of **Cz-Ph-SOXO** and **DCz-DPh-SOXO** blue-shifted to 468 and 475 nm, respectively, which are blue emitters. When introducing the phenyl ring to **CzSOXO**

Table 4 The excitation energies of the S_1 and T_1 states based on S_0 and S_1 geometries and the energy difference between the S_1 and T_1 states for the investigated molecules (in unit of eV)

	S_0 geometry			S_1 geometry			T_1 geometry			Adiabatic
Molecules	S_1	T_1	ΔE_{ST}	S_1	T_1	ΔE_{ST}	S_1	T_1	ΔE_{ST}	ΔE_{ST}
CzSOXO	2.93	2.63	0.30	2.37	2.24	0.13	2.49	1.85	0.64	0.35
DCzSOXO	2.82	2.54	0.28	2.29	2.16	0.13	2.41	1.85	0.56	0.31
Cz-Ph-SOXO	3.11	2.71	0.40	2.65	2.35	0.30	2.75	1.77	0.98	0.63
DCz-DPh-SOXO	3.06	2.68	0.38	2.61	2.33	0.28	2.71	1.77	0.94	0.59

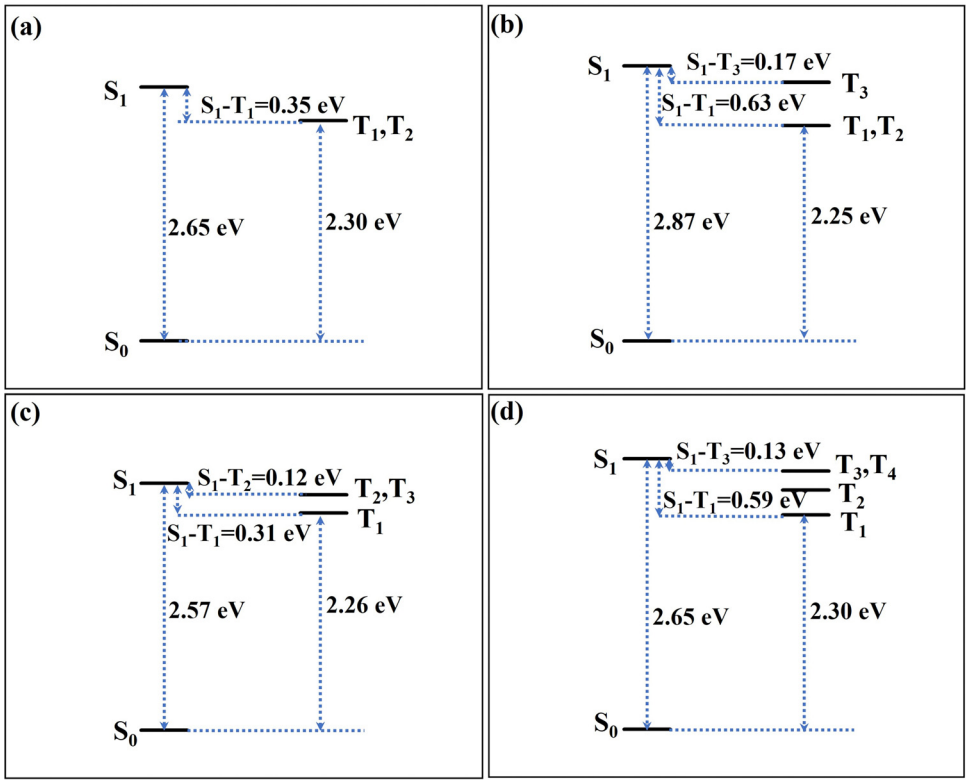

Fig. 5 The energy landscape of the vertical excitation of **CzSOXO** (a), **Cz-Ph-SOXO** (b), **DCzSOXO** (c) and **DCz-DPh-SOXO** (d).

Table 5 The calculated absorption (λ_{ab}) and emission (λ_{em}) wavelengths as well as the oscillator strength based on the PBE0-1/3/6-31G(d) level in a toluene solvent for the investigated molecules (the experimental values are also listed in the parentheses for comparison)

Molecules	λ_{ab} (nm)	f_{VA}	λ_{em} (nm)	f_{VE}
CzSOXO	423 (404[26])	0.0405	524 (536[26])	0.0145
DCzSOXO	440 (406[26])	0.0431	542 (546[26])	0.0157
Cz-Ph-SOXO	399	0.0613	468	0.0622
DCz-DPh-SOXO	405	0.0838	475	0.0665

and **DCzSOXO** between the D and A groups, the oscillator strengths of **Cz-Ph-SOXO** and **DCz-DPh-SOXO** are increased by 1.5 and 2 times, respectively, with respect to those of **CzSOXO** and **DCzSOXO** for the absorption process. While for the emission process, the oscillator strengths of **Cz-Ph-SOXO** and **DCz-DPh-SOXO** are also enhanced by 6 times than those of **CzSOXO** and **DCzSOXO**. From the perspective of oscillator strengths, it can be determined that the designed molecules (**Cz-Ph-SOXO** and **DCz-DPh-SOXO**) possess much better TADF properties compared with the experimental molecules (**CzSOXO** and **DCzSOXO**). Therefore, incorporating the phenyl ring between D and A moieties could be an efficient way for designing new efficient SOXO-based TADF molecules.

4.5 Excited state dynamics

For TADF emitters, the rate constants of radiative (k_r) and nonradiative (k_{nr}) processes from the S_1 to S_0 state, as well as the intersystem crossing (k_{ISC}) and reverse intersystem crossing (k_{RISC}) rates play an important role in the dynamic process of the excited states. It is widely known that the ISC and RISC processes are related to not only the adiabatic energy gap between the S_1 and T_1 states, but also the SOC between the singlet and triplet states. The SOC constants between the S_1 and T_1 (T_2, T_3 and T_4) states are calculated based on the S_1 geometries through the Dalton[66,67] package, as shown in Table 6. The k_r and k_{nr} from the S_1 to S_0 state as well as k_{ISC} and k_{RISC} between the S_1 and T_1 (T_2, T_3 and T_4) states in toluene are provided in Table 7. The radiative decay rates of **CzSOXO** and **DCzSOXO** are 3.52×10^6 and 3.56×10^6 s^{-1}, respectively. While this value for **Cz-Ph-SOXO** and **DCz-DPh-SOXO** is increased to 1.89×10^7 and 1.96×10^7 s^{-1}, respectively, which agrees with the values of oscillator strengths. However, the nonradiative decay rates (k_{nr}) are all larger than the radiative rates (k_r) for **CzSOXO** and **DCzSOXO**, which is not beneficial for the light-emitting process. This is because the nonradiative

Table 6 The spin–orbit coupling (SOC) constants between the S_1 state and the selected triplet states in toluene for the investigated molecules (all the SOC values are in unit of cm^{-1})

Molecules	$\langle S_1\|H_{SO}\|T_1\rangle$	$\langle S_1\|H_{SO}\|T_2\rangle$	$\langle S_1\|H_{SO}\|T_3\rangle$	$\langle S_1\|H_{SO}\|T_4\rangle$
CzSOXO	0.228	0.358	—	—
DCzSOXO	0.215	0.183	0.366	—
Cz-Ph-SOXO	0.158	0.432	0.374	—
DCz-DPh-SOXO	0.141	0.158	0.043	0.365

Table 7 The rate constants of radiative (k_r) and nonradiative (k_{nr}) from the S_1 to S_0 state as well as the ISC (k_{ISC}) and RISC (k_{RISC}) between the S_1 and T_1 (T_2, T_3 and T_4) states in toluene (all the rates are in unit of s^{-1})

Molecules	CzSOXO	DCzSOXO	Cz-Ph-SOXO	DCz-DPh-SOXO
k_r ($S_1 \rightarrow S_0$)	3.52×10^6	3.56×10^6	1.89×10^7	1.96×10^7
k_{nr} ($S_1 \rightarrow S_0$)	5.14×10^{10}	8.40×10^{10}	7.50×10^5	3.83×10^6
k_{ISC} ($S_1 \rightarrow T_1$)	8.27×10^6	1.02×10^6	7.00×10^4	5.65×10^4
k_{RISC} ($T_1 \rightarrow S_1$)	9.89×10^0	1.80×10^0	6.58×10^{-5}	1.82×10^{-2}
k_{ISC} ($S_1 \rightarrow T_2$)	2.06×10^7	2.53×10^6	5.09×10^5	1.59×10^4
k_{RISC} ($T_2 \rightarrow S_1$)	2.39×10^1	6.82×10^2	3.01×10^{-4}	6.32×10^{-5}
k_{ISC} ($S_1 \rightarrow T_3$)	—	1.01×10^7	5.56×10^5	1.43×10^3
k_{RISC} ($T_3 \rightarrow S_1$)	—	2.92×10^3	1.41×10^6	2.66×10^4
k_{ISC} ($S_1 \rightarrow T_4$)	—	—	—	1.02×10^5
k_{RISC} ($T_4 \rightarrow S_1$)	—	—	—	2.50×10^6

process is sensitive to the environment, and the calculated results are based on the single molecule model and without considering the intermolecular interaction. So when made into OLEDs, the nonradiative rates of the designed molecules can be reduced significantly than the calculated values as illustrated in previous studies.[70–72] While k_{nr} of **Cz-Ph-SOXO** and **DCz-DPh-SOXO** is significantly decreased compared with k_r, which is beneficial for the light-emitting process. It is also found in Table 6 that the calculated SOC values between the S_1 state and the triplet state closest to the S_1 state are larger than those values between the S_1 and other triplet states.

For **CzSOXO**, the T_1 and T_2 states are degenerate, and both the T_1 and T_2 states participate in the ISC and RISC processes. The k_{ISC} (2.06×10^7 s^{-1}) and k_{RISC} (2.39×10^1 s^{-1}) between the S_1 and T_2 states are more effective than those between the S_1 and T_1 states due to the larger SOC values between the S_1 and T_2 states. It can be seen in Table 7 that the T_1, T_2 and T_3 states of **DCzSOXO** are all involved in the ISC and RISC processes. The most efficient route of the ISC and RISC processes for **DCzSOXO** is between the S_1 and T_3 states, and k_{ISC} and k_{RISC} are 1.01×10^7 s^{-1} and 2.92×10^3 s^{-1}, respectively. It can also be found in Fig. 5 that the T_2 and T_3 states of **DCzSOXO** are degenerate. However, the energy gap between T_1 and T_2 (T_3) states is as small as 0.19 eV, so the internal conversion process will occur quickly from the T_2 (T_3) to the T_1 state, and the RISC process might also happen from the T_1 to S_1 state. For **Cz-Ph-SOXO** and **DCz-DPh-SOXO**, k_{ISC} values of the most effective route are decreased to 5.56×10^5 and 1.02×10^5 s^{-1}, respectively. However, k_{RISC} values of **Cz-Ph-SOXO** (1.41×10^6 s^{-1}) and **DCz-DPh-SOXO** (2.50×10^6 s^{-1}) of the most effective routes are significantly increased compared with those of **CzSOXO** (2.39×10^1 s^{-1}) and **DCzSOXO** (2.92×10^3 s^{-1}), demonstrating that **Cz-Ph-SOXO** and **DCz-DPh-SOXO** are more facilitated to the occurrence of the RISC process. It can also be found that the RISC from the T_1 (T_2) to S_1 state is very small for **Cz-Ph-SOXO**, which is due to the larger energy gap (0.46 eV) between the T_3 and T_1 (T_2) states. Therefore, the internal conversion process from the T_3 to T_1 (T_2) state will be slow and the RISC process for **Cz-Ph-SOXO** mainly occurs from the T_3 to S_1 state. Similarly, for **DCz-DPh-SOXO**, the energy gap between T_3 (T_4) and T_1 states is also as large as 0.46 eV, so the main ISC and RISC processes have happened between the S_1 and T_3 (T_4) states.

In addition, the phosphorescence rates (k_p) from the T_1 to S_0 states calculated through MOMAP[60–65] software for all the investigated molecules are presented in Table S1 (ESI†). It can be found that the values of k_{RISC} are apparently much larger than the corresponding k_p, indicating that the reverse intersystem crossing process can successfully compete with the phosphorescence process. Based on the analysis of the dynamics of the excited states, it can be concluded that the designed molecules **Cz-Ph-SOXO** and **DCz-DPh-SOXO** with high k_r and efficient k_{RISC} can be used as excellent TADF emitters. Therefore, incorporating phenyl units into D–A and D–A–D type molecules is a good strategy for developing new efficient SOXO-based TADF emitters, and the emission color can also be modulated from green to blue simply by introducing the phenyl ring.

5. Conclusions

In summary, the photophysical processes and excited state dynamics of four SOXO-based molecules are investigated based on the first principles calculation. It is found that incorporating phenyl units between the donor and acceptor groups and changing the molecular types can significantly modulate the excited state properties of these molecules. The TADF mechanisms of the studied molecules are revealed by calculating k_r, k_{nr}, k_{ISC} and k_{RISC}, ΔE_{ST} and SOC based on the thermal vibration correlation function method and TD-DFT approach. Results show that the emission wavelengths of **Cz-Ph-SOXO** and **DCz-DPh-SOXO** are also modulated from green to blue by simply inserting the phenyl ring between the donor and acceptor groups. For the designed molecules **Cz-Ph-SOXO** and **DCz-DPh-SOXO**, the k_r values increased significantly compared with those of **CzSOXO** and **DCzSOXO**. The k_{ISC} values of **Cz-Ph-SOXO** and **DCz-DPh-SOXO** are relatively smaller than those of **CzSOXO** and **DCzSOXO**. However, the k_{RISC} values of **Cz-Ph-SOXO** and **DCz-DPh-SOXO** are significantly increased compared with those of **CzSOXO** and **DCzSOXO**, demonstrating that **Cz-Ph-SOXO** and **DCz-DPh-SOXO** are more facilitated to achieve the TADF process. In particular, the k_{RISC} values of **Cz-Ph-SOXO** and **DCz-DPh-SOXO** reached up to 1.41×10^6 s^{-1} and 2.50×10^6 s^{-1}, respectively, which is beneficial to the occurrence of delayed fluorescence. Our results would be helpful for developing new SOXO-based TADF materials experimentally.

Conflicts of interest

The authors have no conflicts to disclose.

Acknowledgements

This work was supported by the Natural Science Foundation of Shandong, China, Grant No. ZR2020QB074, the National Natural Science Foundation of China, Grant No. 21503056, the Fundamental Research Funds for the Central Universities, Grant No. HIT. NSRIF. 2016090. The authors gratefully acknowledge HZWTECH for providing computational facilities.

References

1 Q. Zhang, J. Li, K. Shizu, S. Huang, S. Hirata, H. Miyazaki and C. Adachi, *J. Am. Chem. Soc.*, 2012, **134**, 14706–14709.
2 H. Uoyama, K. Goushi, K. Shizu, H. Nomura and C. Adachi, *Nature*, 2012, **492**, 234–238.
3 J. Li, T. Nakagawa, J. MacDonald, Q. Zhang, H. Nomura, H. Miyazaki and C. Adachi, *Adv. Mater.*, 2013, **25**, 3319–3323.
4 Y. Im, M. Kim, Y. J. Cho, J. A. Seo, K. S. Yook and J. Y. Lee, *Chem. Mater.*, 2017, **29**, 1946–1963.
5 T. Hofbeck, U. Monkowius and H. Yersin, *J. Am. Chem. Soc.*, 2015, **137**, 399–404.
6 S. Hirata, Y. Sakai, K. Masui, H. Tanaka, S. Y. lee, H. Nomura, N. Nakamura, M. Yasumatsu, H. Nakanotani, Q. S. Zhang, K. Shizu, H. Miyazaki and C. Adachi, *Nat. Mater.*, 2015, **14**, 330–336.
7 H. T. Sun, Z. B. Hu, C. Zhong, X. K. Chen, Z. R. Sun and J.-L. Brédas, *J. Phys. Chem. Lett.*, 2017, **8**, 2393–2398.
8 K. Kawasumi, T. Wu, T. Y. Zhu, H. S. Chae, T. V. Voorhis, M. A. Baldo and T. M. Swager, *J. Am. Chem. Soc.*, 2015, **137**, 11908–11911.
9 Y. Tao, K. Yuan, T. Chen, P. Xu, H. Li, R. Chen, C. Zheng, L. Zhang and W. Huang, *Adv. Mater.*, 2014, **26**, 7931–7958.
10 G. Mehes, H. Nomura, Q. Zhang, T. Nakagawa and C. Adachi, *Angew. Chem., Int. Ed.*, 2012, **51**, 11311–11315.
11 S. Y. Lee, T. Yasuda, H. Nomura and C. Adachi, *Appl. Phys. Lett.*, 2012, **101**, 093306.
12 T. Nakagawa, S. Y. Ku, K. T. Wong and C. Adachi, *Chem. Commun.*, 2012, **48**, 9580–9582.
13 H. Nakanotani, K. Masui, J. Nishide, T. Shibata and C. Adachi, *Sci. Rep.*, 2013, **3**, 2127.
14 H. Tsujimoto, D.-G. Ha, G. Markopoulos, H. S. Chae, M. A. Baldo and T. M. Swager, *J. Am. Chem. Soc.*, 2017, **139**, 4894–4900.
15 A. E. Nikolaenko, M. Cass, F. Bourcet, D. Mohamad and M. Roberts, *Adv. Mater.*, 2015, **27**, 7236–7240.
16 P. Rajamalli, N. Senthilkumar, P. Gandeepan, P. Y. Huang, M. J. Huang, C. Z. Ren-Wu, C. Y. Yang, M. J. Chiu, L. K. Chu, H. W. Lin and C. H. Cheng, *J. Am. Chem. Soc.*, 2016, **138**, 628–634.
17 T. Hatakeyama, K. Shiren, K. Nakajima, S. Nomura, S. Nakatsuka, K. Kinoshita, J. Ni, Y. Ono and T. Ikuta, *Adv. Mater.*, 2016, **28**, 2777–2781.
18 T. A. Lin, T. Chatterjee, W. L. Tsai, W. K. Lee, M. J. Wu, M. Jiao, K. C. Pan, C. L. Yi, C. L. Chung, K. T. Wong and C. C. Wu, *Adv. Mater.*, 2016, **28**, 6976–6983.
19 M. Numata, T. Yasuda and C. Adachi, *Chem. Commun.*, 2015, **51**, 9443–9446.
20 X. K. Chen, Y. Tsuchiya, Y. Ishikawa, C. Zhong, C. Adachi and J.-L. Brédas, *Adv. Mater.*, 2017, **29**, 1702767.
21 Q. Zhu, X. Guo and J. Zhang, *J. Comput. Chem.*, 2019, **40**, 1578–1585.
22 L. J. Wang, T. Li, P. C. Feng and Y. Song, *Phys. Chem. Chem. Phys.*, 2017, **19**, 21639–21647.
23 Y. C. Li, Z. H. Wang, X. L. Li, G. Z. Xie, D. C. Chen, Y. F. Wang, C. C. Lo, A. Lien, J. B. Peng, Y. Cao and S. J. Su, *Chem. Mater.*, 2015, **27**, 1100–1109.
24 X. F. Lu, S. H. Fan, J. H. Wu, X. W. Jia, Z. S. Wang and G. Zhou, *J. Org. Chem.*, 2014, **79**, 6480–6489.
25 P. Data, P. Pander, M. Okazaki, Y. Takeda, S. Minakata and A. P. Monkman, *Angew. Chem., Int. Ed.*, 2016, **55**, 5739–5744.
26 M. K. Etherington, F. Franchell, J. Gibson, T. Northey, J. Santos, J. S. Ward, H. F. Higginbotham, P. Data, A. Kurowska, P. L. D. Santos, D. R. Graves, A. S. Batsaov, F. B. Dias, M. R. Bryce, T. J. Penfold and A. P. Monkman, *Nat. Commun.*, 2017, **8**, 14987.
27 Z. H. Wang, Y. C. Li, X. Y. Cai, D. C. Chen, G. Z. Xie, K. K. Liu, Y. C. Wu, C. C. Lo, A. Lien, Y. Cao and S. J. Su, *ACS Appl. Mater. Interfaces*, 2016, **8**, 8627–8636.
28 J. B. Im, R. Lampande, G. H. Kim, J. Y. Lee and J. H. Kwon, *J. Phys. Chem. C*, 2017, **121**, 1305–1314.
29 C. C. Fan, C. B. Duan, C. M. Han, B. Han and H. Xu, *ACS Appl. Mater. Interfaces*, 2016, **8**, 27383–27393.
30 C. Wang, X. L. Li, Y. Y. Pan, S. T. Zhang, L. Yao, Q. Bai, W. J. Li, P. Lu, B. Yang, S. J. Su and Y. G. Ma, *ACS Appl. Mater. Interfaces*, 2016, **8**, 3041–3049.
31 S. Y. Lee, C. Adachi and T. Yasuda, *Adv. Mater.*, 2016, **28**, 4626–4631.
32 S. Ishijima, M. Higashi and H. Yamaguchi, *J. Phys. Chem.*, 1994, **98**, 10432–10435.
33 C. Ley, F. Morlet-Savary, P. Jacques and J. P. Fouassier, *Chem. Phys.*, 2000, **255**, 335–346.
34 A. M. Turek, G. Krishnamoorthy, K. Phipps and J. Saltiel, *J. Phys. Chem. A*, 2002, **106**, 6044–6052.
35 S. Reineke and M. A. Baldo, *Sci. Rep.*, 2014, **4**, 3797.
36 H. Wang, L. S. Xie, Q. Peng, L. Q. Meng, Y. Wang, Y. P. Yi and P. F. Wang, *Adv. Mater.*, 2014, **26**, 5198–5204.
37 X. F. Wei, Y. Z. Chen, R. H. Duan, J. J. Liu, R. F. Wang, Y. W. Liu, Z. Y. Li, Y. P. Yi, Y. Y. Takamura, P. F. Wang and Y. Wang, *J. Mater. Chem. C*, 2017, **5**, 12077–12084.
38 X. Wei, Z. Li, T. Hu, R. Duan, J. Liu, R. Wang, Y. Liu, X. Hu, Y. Yi, P. Wang and Y. Wang, *Adv. Opt. Mater.*, 2019, **7**, 1801767.
39 Y. C. Li, X. L. Li, D. J. Chen, X. Y. Cai, G. Z. Xie, Z. Z. He, Y. C. Wu, A. Lien, Y. Cao and S. J. Su, *Adv. Funct. Mater.*, 2016, **26**, 6904–6912.

40 M. Y. Wong and E. Zysman-Colman, *Adv. Mater.*, 2017, **29**, 1605444.
41 Z. Tu, G. Han, T. Hu, R. Duan and Y. Yi, *Chem. Mater.*, 2019, **31**, 6665–6671.
42 Q. Lu, M. Qin, S. Liu, L. Lin, C.-K. Wang, J. Fan and Y. Song, *Chem. Phys. Lett.*, 2021, **764**, 138260.
43 Y. Liu, L. Wang, L. Xu and Y. Song, *J. Mater. Chem. C*, 2023, **11**, 13403–13417.
44 Q. Lu, G. Y. Jiang, F. Y. Li, L. L. Lin, C. K. Wang, J. Z. Fan and Y. Z. Song, *Spectrochim. Acta, Part A*, 2020, **229**, 117964.
45 Q. Peng, D. Fan, R. H. Duan, Y. P. Yi, Y. L. Niu, D. Wang and Z. G. Shuai, *J. Phys. Chem. C*, 2017, **121**, 13448–13456.
46 Q. Peng, Y. L. Niu, Q. Shi, X. Gao and Z. G. Shuai, *J. Chem. Theory Comput.*, 2013, **9**, 1132–1143.
47 Y. L. Niu, Q. Peng, C. M. Deng, X. Gao and Z. G. Shuai, *J. Phys. Chem. A*, 2010, **114**, 7817–7831.
48 B. Miehlich, A. Savin, H. Stoll and H. Preuss, *Chem. Phys. Lett.*, 1989, **157**, 200–206.
49 C. Adamo and V. Barone, Toward Reliable Density Functional Methods without Adjustable Parameters: The PBE0 Model, *J. Chem. Phys.*, 1999, **110**, 6158–6170.
50 C. A. Guido, E. Bremond, C. Adamo and P. Cortona, *J. Chem. Phys.*, 2013, **138**, 021104.
51 A. D. Boese and J. M. L. Martin, *J. Chem. Phys.*, 2004, **121**, 3405–3416.
52 Y. Zhao and D. G. Truhlar, *Theor. Chem. Acc.*, 2008, **120**, 215–241.
53 T. Yanai, D. P. Tew and N. C. Handy, *Chem. Phys. Lett.*, 2004, **393**, 51–57.
54 Y.-S. Lin, G.-D. Li, S.-P. Mao and J.-D. Chai, *J. Chem. Theory Comput.*, 2013, **9**, 263–272.
55 H. Ma, W. Shi, J. Ren, W. Li, Q. Peng and Z. Shuai, *J. Phys. Chem. Lett.*, 2016, **7**, 2893–2898.
56 J. Liu, J. Fan, K. Zhang, Y. Zhang, C.-K. Wang and L. Lin, *Chin. Phys. B*, 2020, **29**, 088504.
57 Q. Peng, Y. Yi, Z. Shuai and J. Shao, *J. Chem. Phys.*, 2007, **126**, 114302.
58 J. Tomasi, B. Mennucci and R. Cammi, *J. Cheminform.*, 2005, **105**, 2999–3093.
59 M. J. Frisch, G. W. Trucks, H. B. Schlegel, G. E. Scuseria, M. A. Robb, J. R. Cheeseman, G. Scalmani, V. Barone, B. Mennucci, G. A. Petersson, H. Nakatsuji, M. Caricato, X. Li, H. P. Hratchian, A. F. Izmaylov, J. Bloino, G. Zheng, J. L. Sonnenberg, M. Hada, M. Ehara, K. Toyota, R. Fukuda, J. Hasegawa, M. Ishida, T. Nakajima, Y. Honda, O. Kitao, H. Nakai, T. Vreven, J. A. Montgomery Jr, J. E. Peralta, F. Ogliaro, M. Bearpark, J. J. Heyd, E. Brothers, K. N. Kudin, V. N. Staroverov, R. Kobayashi, J. Normand, K. Raghavachari, A. Rendell, J. C. Burant, S. S. Iyengar, J. Tomasi, M. Cossi, N. Rega, J. M. Millam, M. Klene, J. E. Knox, J. B. Cross, V. Bakken, C. Adamo, J. Jaramillo, R. Gomperts, R. E. Stratmann, O. Yazyev, A. J. Austin, R. Cammi, C. Pomelli, J. W. Ochterski, R. L. Martin, K. Morokuma, V. G. Zakrzewski, G. A. Voth, P. Salvador, J. J. Dannenberg, S. Dapprich, A. D. Daniels, Ö. Farkas, J. B. Foresman, J. V. Ortiz, J. Cioslowski and D. J. Fox, *Gaussian 09, Revision D.01*, Gaussian Inc., Wallingford, CT, 2010.
60 Y. L. Niu, W. Q. Li, Q. Peng, H. Geng, Y. P. Yi, L. J. Wang, G. J. Nan, D. Wang and Z. G. Shuai, *Mol. Phys.*, 2018, **116**, 1078–1090.
61 Q. Peng, Y. P. Yi, Z. G. Shuai and J. S. Shao, *J. Am. Chem. Soc.*, 2007, **129**, 9333–9339.
62 Y. L. Niu, Q. Peng and Z. G. Shuai, *Sci. China Ser. B-Chem.*, 2008, **51**, 1153–1158.
63 Z. G. Shuai, *Chin. J. Chem.*, 2020, **38**, 1223–1232.
64 Z. G. Shuai and Q. Peng, *Phys. Rep.*, 2014, **537**, 123–156.
65 Z. G. Shuai and Q. Peng, *Nat. Sci. Rev.*, 2017, **4**, 224–239.
66 DALTON. A molecular electronic structure program, Release Dalton 2019. Alpha, 2019, **https://daltonprogram.org/**.
67 K. Aidas, C. Angeli, K. L. Bak, V. Bakken, R. Bast, L. Boman, O. Christiansen, R. Cimiraglia, S. Coriani, P. Dahle, E. K. Dalskov, U. Ekström, T. Enevoldsen, J. J. Eriksen, P. Ettenhuber, B. Fernández, L. Ferrighi, H. Fliegl, L. Frediani, K. Hald, A. Halkier, C. Hättig, H. Heiberg, T. Helgaker, A. C. Hennum, H. Hettema, E. Hjertenæs, S. Høst, I.-M. Høyvik, M. F. Iozzi, B. Jansik, H. J. A. Jensen, D. Jonsson, P. Jørgensen, J. Kauczor, S. Kirpekar, T. Kjærgaard, W. Klopper, S. Knecht, R. Kobayashi, H. Koch, J. Kongsted, A. Krapp, K. Kristensen, A. Ligabue, O. B. Lutnæs, J. I. Melo, K. V. Mikkelsen, R. H. Myhre, C. Neiss, C. B. Nielsen, P. Norman, J. Olsen, J. M. H. Olsen, A. Osted, M. J. Packer, F. Pawlowski, T. B. Pedersen, P. F. Provasi, S. Reine, Z. Rinkevicius, T. A. Ruden, K. Ruud, V. Rybkin, P. Salek, C. C. M. Samson, A. Sánchez de Merás, T. Saue, S. P. A. Sauer, B. Schimmelpfennig, K. Sneskov, A. H. Steindal, K. O. Sylvester-Hvid, P. R. Taylor, A. M. Teale, E. I. Tellgren, D. P. Tew, A. J. Thorvaldsen, L. Thøgersen, O. Vahtras, M. A. Watson, D. J. D. Wilson, M. Ziolkowski and H. Ågren, *Wiley Interdiscip. Rev.: Comput. Mol. Sci.*, 2014, **4**, 269–284.
68 T. Lu and F. W. Chen, *J. Comput. Chem.*, 2012, **33**, 580–592.
69 Z. Y. Liu, T. Lu and Q. X. Chen, *Carbon*, 2020, **165**, 461–467.
70 J. Leng, Z. Zhang, Y. Zhang, J. Sun and H. Ma, *J. Lumin.*, 2018, **204**, 312–318.
71 J. Fan, L. Cai, L. Lin and C.-K. Wang, *Phys. Chem. Chem. Phys.*, 2017, **19**, 29872–29879.
72 B. Liu, H. Nie, X. Zhou, S. Hu, D. Luo, D. Gao, J. Zou, M. Xu, L. Wang, Z. Zhao, A. Qin, J. Peng, H. Ning, Y. Cao and B. Z. Tang, *Adv. Funct. Mater.*, 2016, **26**, 776–783.

